JACS
JOURNAL OF THE AMERICAN CHEMICAL SOCIETY
Communication
pubs.acs.org/JACS

The Nature of Lithium Battery Materials under Oxygen Evolution Reaction Conditions

Seung Woo Lee,[†,‡] Christopher Carlton,[†] Marcel Risch,[†] Yogesh Surendranath,[‡] Shuo Chen,[†] Sho Furutsuki,[§] Atsuo Yamada,[§] Daniel G. Nocera,*[,‡] and Yang Shao-Horn*[,†]

[†]Department of Mechanical Engineering and [‡]Department of Chemistry, Massachusetts Institute of Technology, Cambridge, Massachusetts 02139, United States

[§]Department of Chemical System Engineering, The University of Tokyo, 7-3-1 Hongo, Bunkyo-ku, Tokyo 113-8656, Japan

Supporting Information

ABSTRACT: Transition-metal oxide and phosphate materials, commonly used for lithium battery devices, are active as oxygen evolution reaction (OER) catalysts under alkaline and neutral solution conditions. Electrodes composed of $LiCoO_2$ and $LiCoPO_4$ exhibit progressive deactivation and activation for OER catalysis, respectively, upon potential cycling at neutral pH. The deactivation of $LiCoO_2$ and activation of $LiCoPO_4$ are coincident with changes in surface morphology and composition giving rise to spinel-like and amorphous surface structures, respectively. The amorphous surface structure of the activated $LiCoPO_4$ is compositionally similar to that obtained from the electrodeposition of cobalt oxide materials from phosphate-buffered electrolyte solutions. These results highlight the importance of a combined structural and electrochemical analysis of the materials surface when assessing the true nature of the OER catalyst.

Water splitting to form H_2 and O_2 is a key enabling process for the storage of solar or electrical renewable energy in the form of chemical fuels.[1] This process involves the four-proton, four-electron oxidation of water to O_2 and concomitant two-proton, two-electron reduction of the generated protons to H_2. The oxygen evolution reaction (OER) is often rate-limiting because of the sluggish kinetics associated with O−H bond breaking and attendant O═O bond formation and the need to perform proton-coupled electron transfer chemistry at the high equivalency of 4.[2] In addition, gas evolution may erode electrocatalysts, particularly for nanoparticles upon water splitting. The design of active and durable OER catalysts therefore represents a major challenge in the construction of efficient solar-to-fuels energy conversion and storage devices.

Oxides of first-row transition metals, such as the edge-sharing octahedral spinels,[3] can exhibit OER activities in alkaline solution that are comparable to those of RuO_2 and IrO_2.[4] Additionally, perovskites containing ions of late-first-row transition metals (e.g., Ni and Co) also exhibit high OER activities in alkaline solution.[5] Similarly high activities may be achieved from cobalt and nickel oxide materials that are electrodeposited from solution in the presence of electrolyte under neutral or near-neutral conditions.[6] Extended X-ray absorption fine structure studies have shown that these electrodeposited Co catalysts are amorphous with a structural motif of multimetal centers in edge-sharing octahedra.[7] Mechanistic studies have revealed that the OER activity per Co atom decreases with increasing size of the cobalt oxide clusters, which has been attributed to a decrease in the number of active sites for OER.[8] Extending this logic to submicrometer-scale oxide particles would suggest that conventional oxide catalysts should have much lower OER activities per Co than the bulk-active films.

In this work, we examined and compared the OER activities of submicrometer-sized particles of Co-based extended solids, $LiCoO_2$ with edge-sharing octahedra and olivine $LiCoPO_4$ with corner-sharing octahedra in bulk (Figures S1−S3 in the Supporting Information), at pH 7 and 13. We found that the OER activity and surface morphology and composition of submicrometer-sized particles change significantly upon potential cycling in the region of oxygen evolution, as revealed by high-resolution transmission electron microscopy (HRTEM) and scanning transmission electron microscopy (STEM). By correlating the structure and chemical changes in the near-surface region with OER activity, we found that the surface-restructured form of an extended solid catalyst, rather than the initial bulk phase, defines its steady-state performance.

Cyclic voltammetry (CV) scans of thin films of $LiCoO_2$ and $LiCoPO_4$ supported on glassy carbon electrodes (GCEs) in an aqueous 0.1 M potassium phosphate (KP_i) electrolyte at pH 7.0 are shown in Figure 1 (Ohmically corrected current) and Figure S4 (raw data before correction). The first CV scan of $LiCoO_2$ (Figure 1a) showed a large oxidation peak with an onset potential of ∼1.3 V vs reversible hydrogen electrode (RHE) that is ascribed to oxidation of $LiCoO_2$ in aqueous solution with concomitant delithiation.[9] A second oxidation wave with an onset potential of 1.6 V vs RHE is ascribed to the OER from water. Upon subsequent potential cycling from 1.2 to 1.8 V vs RHE, the OER current gradually decreased and approached a stable value after 100 cycles, indicative of catalyst deactivation. In contrast, the first CV scan of $LiCoPO_4$ showed only the oxidation wave associated with the OER at an onset potential of ∼1.6 V vs RHE (Figure 1b). The OER current increased during subsequent potential cycling and attained a stable value after 100 cycles, indicative of catalyst activation.

The OER activities of $LiCoO_2$ and $LiCoPO_4$ extracted from CV scans at pH 7 are shown in Figure 2. Activities normalized to

Received: August 6, 2012
Published: October 3, 2012

   dx.doi.org/10.1021/ja307814j | J. Am. Chem. Soc. 2012, 134, 16959−16962

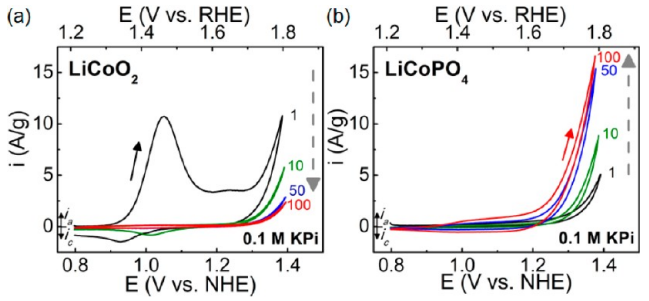

Figure 1. CV scans of (a) $LiCoO_2$ and (b) $LiCoPO_4$ electrodes at a scan rate of 10 mV/s at 900 rpm in 0.1 M KP_i electrolyte at pH 7.0. Dashed arrows indicate the progression upon successive cycling, and number labels show the number of cycles. The OER current was Ohmically corrected using the measured ionic resistance (~65 Ω). The oxide ($LiCoO_2$ or $LiCoPO_4$) loading was 0.10 mg/cm^2 of GCE.

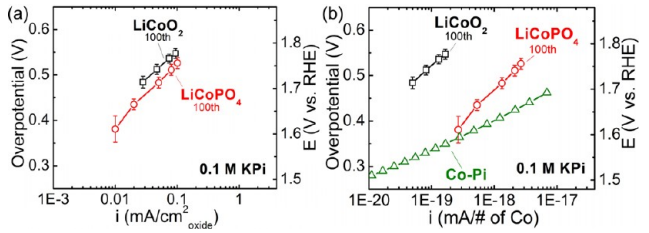

Figure 2. Tafel plots for $LiCoO_2$ (black □) and $LiCoPO_4$ (red ○) for the 100th cycle normalized to (a) the initial surface area of oxide particles and (b) the total number of Co atoms in 0.1 M KP_i electrolyte at pH 7. Data for oxidic Co films electrodeposited from phosphate electrolyte (Co−P_i films)[10] (green △) are included in (b) for comparative purposes. Tafel plots for $LiCoO_2$ and $LiCoPO_4$ were constructed by averaging the currents of the forward and reverse CV scans. Error bars indicate the standard deviation of three separate measurements of independently prepared electrodes. The specific areas of $LiCoO_2$ and $LiCoPO_4$ are 1.07 and 9.96 m^2/g, respectively. The Tafel plot of Co−P_i (24 mC/cm^2) was determined potentiometrically.[10]

the particle surface area (yielding an estimate of specific activity) and the total number of Co atoms are shown in Figure 2a,b, respectively. The OER activities normalized to the geometric area of the substrate are compared in Figure S5a. The OER activity plots shown in Figure 2 were constructed by averaging the currents from the forward and reverse CV scans. Thus, the calculated OER current does not represent a true catalytic steady state and may contain pseudocapacitive contributions. Nevertheless, the calculated currents are expected to provide a reasonable approximation of the true steady-state current, as potentiostatic electrolysis of $LiCoPO_4$ at 1.7 V vs RHE (Figure S6) yielded a similar mass-normalized value. Interestingly, other olivine compounds, $LiFePO_4$ and $LiMnPO_4$, showed reduction of current during CV cycling and gradually approached values much smaller than that of $LiCoPO_4$ (Figure S7).

Though the estimated specific OER activities of $LiCoO_2$ and $LiCoPO_4$ are comparable (Figure 2a), the OER activity of $LiCoPO_4$ per Co atom was larger than that of $LiCoO_2$ by >1 order of magnitude. Such an increase may be attributed to the smaller particle size of $LiCoPO_4$ and amorphization of the surface upon potential cycling (see below). It is interesting to note that the OER activity per Co for $LiCoPO_4$ (~70 nm) after 100 cycles approached that of electrodeposited thin (~200 nm) films of Co−P_i (Figure 2b). The Tafel slopes of $LiCoO_2$ and $LiCoPO_4$ were found to be ~120 mV/decade. This slope is significantly higher than the slope of ~60 mV/decade observed for thin Co−P_i films.[10] However, for the Co−P_i films, the Tafel slope has been shown to increase to 110 mV/decade with increasing film thickness, suggesting that limitations on ion or electron transport through the film artificially inflate the Tafel slope relative to the activation-controlled value.[10,11] We postulate that similar transport resistances may give rise the high apparent Tafel slopes in these materials, which are not reflective of the activation-controlled kinetics of the OER.

CV cycles of $LiCoO_2$ and $LiCoPO_4$ electrodes in an aqueous 0.1 M KOH at pH 13 are shown in Figure 3. Similar to the data

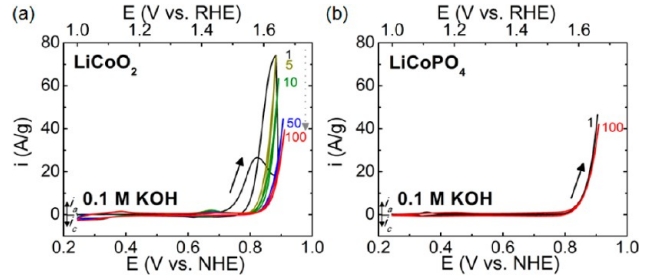

Figure 3. CV scans of (a) $LiCoO_2$ and (b) $LiCoPO_4$ electrodes at a scan rate of 10 mV/s at 900 rpm in 0.1 M KOH at pH 13. Data for 100 continuous cycles taken without pause are shown. The OER current was Ohmically corrected using the measured ionic resistance (~40 Ω). The oxide ($LiCoO_2$ or $LiCoPO_4$) loading was 0.10 mg/cm^2 of GCE.

collected at pH 7, $LiCoO_2$ shows a characteristic peak associated with oxidation of $LiCoO_2$ at an onset potential of ~1.4 V vs RHE (found only in the first cycle) and an OER wave with an onset potential of ~1.6 V vs RHE. The OER activity was found to decrease gradually and approach a stable value after 100 cycles. In contrast, $LiCoPO_4$ in KOH showed only an OER wave with an onset potential of ~1.6 V vs RHE, which remained nearly constant in subsequent CV scans.

Quasi-steady-state OER activities of $LiCoO_2$ and $LiCoPO_4$ from CV scans at pH 13 normalized to the particle surface area (yielding an estimate of specific activity) and the total number of Co atoms are shown in Figure 4a,b, respectively. The OER activities were also normalized to the geometric area of the substrate (see Figure S8a). $LiCoO_2$ exhibits a higher specific OER activity than $LiCoPO_4$ (Figure 4a), whereas the OER activities per Co atom for these compounds were comparable because of the larger specific surface area and smaller particle size

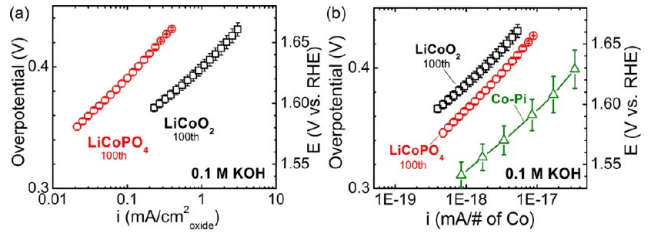

Figure 4. Tafel plots for $LiCoO_2$ (100th cycle; black □), $LiCoPO_4$ (100th cycle; red ○), and electrodeposited Co−P_i (green △) at 900 rpm normalized to (a) the surface area of oxide particles and (b) the total number of Co atoms in 0.1 M KOH electrolyte at pH 13. The Tafel plots of $LiCoO_2$ and $LiCoPO_4$ were constructed by averaging the currents of the forward and reverse CV scans (10 mV/s). The specific areas of $LiCoO_2$ and $LiCoPO_4$ are 1.07 m^2/g and 9.96 m^2/g, respectively. The Tafel plot of Co−P_i (24 mC/cm^2) was determined by galvanostatic experiments. All error bars indicate the standard deviation of three measurements.

dx.doi.org/10.1021/ja307814j | J. Am. Chem. Soc. 2012, 134, 16959−16962

of $LiCoPO_4$. The OER activity per Co in $LiCoPO_4$ after 100 cycles was ~5 times lower than those of Co−P_i films (Figure 4b). In contrast to the data obtained under neutral conditions, nearly identical slopes of ~60 mV/decade were observed.

The OER deactivation of $LiCoO_2$ and activation of $LiCoPO_4$ upon potential scanning suggested the possibility of structural and chemical changes. Consistent with this possibility, considerable changes in the pseudocapacitive currents during cycling were observed for $LiCoO_2$ and $LiCoPO_4$ at pH 7 and 13: those of $LiCoO_2$ gradually decreased (Figure S9a,c), whereas those of $LiCoPO_4$ increased (Figure S9b,d). Cycled $LiCoPO_4$ showed large pseudocapacitive currents and onset OER potentials similar to those of thin films of Co−P_i at pH 7, whereas $LiCoO_2$ exhibited much smaller pseudocapacitive currents (Figure 5a). In contrast, the $LiCoO_2$ and $LiCoPO_4$

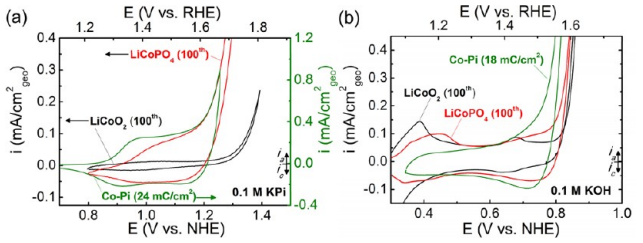

Figure 5. Comparison of CV scans for $LiCoO_2$ (100th cycle), $LiCoPO_4$ (100th cycle), and electrodeposited Co−P_i in (a) 0.1 M KP_i at pH 7[10] and (b) 0.1 M KOH at pH 13. The oxide ($LiCoO_2$ or $LiCoPO_4$) loading was 0.10 mg/cm^2 of GCE. For Co−P_i films, the loadings were 24 mC/cm^2 at 0.1 M KP_i[10] and 18 mC/cm^2 at 0.1 M KOH. The OER current was measured at 10 mV/s and Ohmically corrected.

pseudocapacitive currents and OER onsets were similar to each other and those of Co−P_i after 100 cycles at pH 13 (Figure 5b). The evolution of the pseudocapacitive currents of $LiCoPO_4$ at pH 7 and 13 and $LiCoO_2$ at pH 13 to assume values similar to those of Co−P_i with CV cycling led us to consider that the near-surface region of the lithium cobalt oxides were structurally and chemically transformed into a material akin to Co−P_i.

HRTEM images together with fast Fourier transforms (FFTs) provided direct evidence for structural and chemical changes in the near-surface regions of $LiCoO_2$ and $LiCoPO_4$. Representative HRTEM images of surface regions of pristine $LiCoO_2$ and $LiCoPO_4$ are shown in Figure 6a,d, respectively. Their FFTs can be indexed as the $[2\bar{2}1]$ zone axis in the $R\bar{3}m$ layered structure and the $[\bar{1}02]$ zone axis of the *Pmna* olivine structure. The lattice fringes in the images are visible to the surface boundary with no evidence of an amorphous region. After 100 CV scans at pH 7, the surface region of $LiCoO_2$ remained crystalline but was transformed into a spinel-like structure (Figure 6b and Figure S10), as revealed by FFTs of HRTEM images of cycled $LiCoO_2$ surfaces. For example, the FFT in Figure 6b could not be indexed to the $R\bar{3}m$ space group of $LiCoO_2$ and was instead indexed to the $[01\bar{1}]$ zone axis of an $Fd\bar{3}m$ spinel structure. The FFT reflection intensities suggested the formation of the spinel-like phase $LiCo_2O_4$ (Figure S10) rather than Co_3O_4 because the (200) reflections were less intense than the (111) and (400) reflections, which is not the case for Co_3O_4. This result contrasts with a recent report that spinel $Li_2Co_2O_4$ has a much higher OER activity than layered $LiCoO_2$ at pH 7.2.[12] These differences are not clearly understood because of the lack of information about the actual surface structure of the oxide in the previous study under OER conditions.

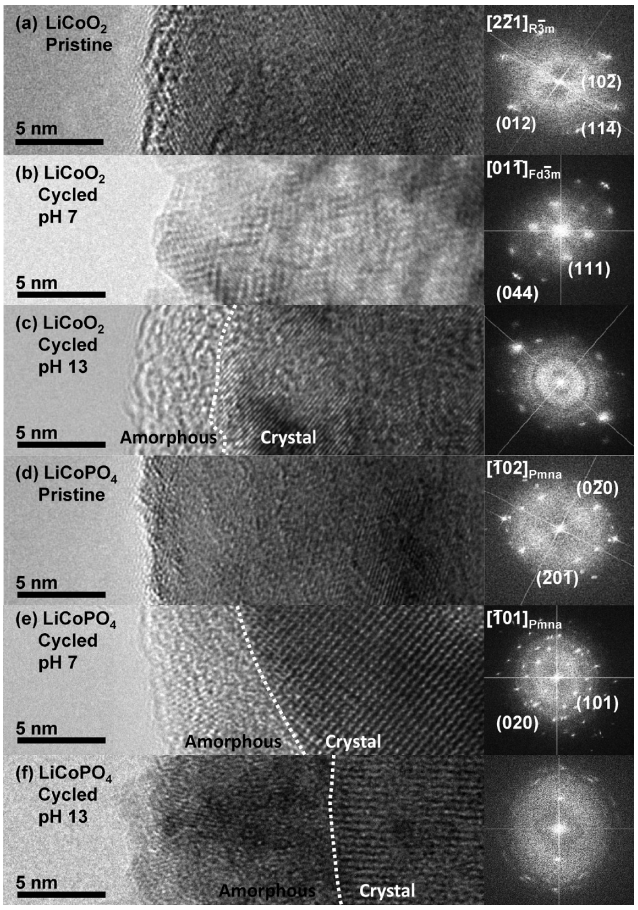

Figure 6. (left) HRTEM images and (right) FFTs of surface regions of $LiCoO_2$ and $LiCoPO_4$: (a) pristine $LiCoO_2$; (b) cycled $LiCoO_2$ in 0.1 M KP_i (pH 7) (Figure 1a); (c) cycled $LiCoO_2$ in 0.1 M KOH (pH 13) (Figure 3a); (d) pristine $LiCoPO_4$; (e) cycled $LiCoPO_4$ in 0.1 M KP_i (pH 7) (Figure 1b); (f) cycled $LiCoPO_4$ in 0.1 M KOH (pH 13) (Figure 3b). White dashed lines indicate the interface between crystalline and amorphous regions. The electrodes were subjected to 100 continuous cycles without pause at a scan rate of 10 mV/s at 900 rpm from 1.2 to 1.8 V vs RHE in 0.1 M KP_i at pH 7 and from 1.0 to 1.7 V vs RHE in 0.1 M KOH at pH 13.

HRTEM images showed that $LiCoPO_4$ was transformed into an amorphous surface phase upon exhaustive cycling at pH 7, as evidenced by the lack of well-defined lattice fringes in the surface region (Figures 6e and S11). This transformation of the surface was further supported by selected-area FFT analysis of cycled $LiCoPO_4$ at pH 7, which confirmed clear differences between the center and surface regions of the material. The FFT from the center region showed spots indicative of well-ordered crystals consistent with the olivine structure, whereas that from the surface region showed a diffuse ring and the absence of FFT spots, characteristic of amorphous materials with no long-range order. Moreover, STEM energy dispersive X-ray spectroscopy (EDS) analysis revealed that the change in the surface to an amorphous material was accompanied by phosphorus leaching from $LiCoPO_4$ during cycling (Figure S11b). Five randomly selected spots from the center crystalline region of the $LiCoPO_4$ electrode showed P/Co ratios close to 50:50. Conversely, selected spots from the amorphous surface region showed a P/Co ratio of 35:65, indicating leaching of P from the surface region. Importantly, the P/Co ratio of ~1:2 in the surface region is in line with the composition of Co oxide films electrodeposited

dx.doi.org/10.1021/ja307814j | J. Am. Chem. Soc. 2012, 134, 16959−16962

from Co^{2+}-containing phosphate electrolyte at neutral pH.[6a,b] HRTEM images revealed that CV cycling of $LiCoO_2$ and $LiCoPO_4$ at pH 13 also led to an amorphous material (Figures 6c and S12). $LiCoPO_4$ exhibited a thicker amorphous region and more pronounced P leaching than at pH 7 (Figures 6f and S13).

The differences in the surface changes of $LiCoO_2$ and $LiCoPO_4$ during CV cycling can be attributed to different oxidation processes of Co ions in $LiCoO_2$ (Co^{3+}/Co^{4+}) and $LiCoPO_4$ ($Co^{2+/3+}$ and Co^{3+}/Co^{4+}).[13] In an oxygen ligand field, Co^{2+} ($t_{2g}^5e_g^2$) is high-spin and substitutionally labile, whereas Co^{3+} ($t_{2g}^6e_g^0$) is low-spin and substitutionally inert.[14,15] We postulate that labile Co^{2+} ($t_{2g}^5e_g^2$) ions may dissociate from the surface in minor equilibrium.[14] Upon potential cycling in phosphate electrolyte, these Co^{2+} ions would readily be redeposited on the surface,[6d] giving rise to an amorphous film compositionally similar to that formed from direct electrodeposition. Indeed, radiolabeling experiments have established that a dissolution/redeposition mechanism is operative for electrodeposited films subject to potential cycling.[14] In line with the hydrated nature of $Co-P_i$ deposits, the amorphous surface of $LiCoPO_4$ exhibited large pseudocapacitive currents during cycling. As $LiCoO_2$ does not access Co^{2+} upon potential cycling, it does not incur a similar changeover to an amorphous phase. Rather, the surface is reconstructed from the layered phase to the spinel phase ($LiCo_2O_4$) during cycling. Unfortunately, the resulting spinel phase lacks the high internal active site density of amorphous $Co-P_i$,[6b,16] accounting for its lower activity.

In contrast to the disparate behavior of $LiCoPO_4$ and $LiCoO_2$ at neutral pH, both materials became amorphous at pH 13, but neither exhibited increased activity. The negligible solubility of Co^{2+} ions at pH 13[17] disfavors a dissolution/redeposition pathway, preventing the formation of a hydrated, amorphous oxide akin to $Co-P_i$. At this extreme pH, it is likely that an alternative mechanism for the amorphous phase change is operative; this remains a subject of continued study.

In summary, we have provided direct evidence for structural and chemical changes of Co-based lithium battery materials during the OER. Upon scanning of the applied potential, the surface of $LiCoO_2$ was converted to a spinel-like $LiCo_2O_4$ structure at pH 7, whereas an amorphous surface layer was obtained at pH 13. In contrast, an amorphous surface layer was generated in $LiCoPO_4$ upon potential cycling at both pH 7 and 13, accompanied by leaching of P from the film. The composition of the amorphous material formed from $LiCoPO_4$ (pH 7) was similar to $Co-P_i$, suggesting a dissolution/redeposition pathway for electrode activation. The results highlight that understanding and controlling surface restructuring should be a focus of catalyst development, as the restructured material defines the catalyst's steady-state performance. The surface reconstruction of perovskite electrocatalysts[5c] under OER conditions (Figure S14) is currently under investigation.

■ ASSOCIATED CONTENT

Supporting Information

Experimental methods and Figures S1–S14. This material is available free of charge via the Internet at http://pubs.acs.org.

■ AUTHOR INFORMATION

Corresponding Author

nocera@mit.edu; shaohorn@mit.edu

Notes

The authors declare no competing financial interest.

■ ACKNOWLEDGMENTS

We thank the NSF MRSEC Program (DMR 0819762) and a Center for Chemical Innovation of the National Science Foundation (grant to D.G.N), CCI Powering the Planet (Grants CHE-0802907 and CHE-0947829, grant to D.G.N.) for support and K. May and K. Bediako for fruitful discussions.

■ REFERENCES

(1) (a) Cook, T. R.; Dogutan, D. K.; Reece, S. Y.; Surendranath, Y.; Teets, T. S.; Nocera, D. G. *Chem. Rev.* **2010**, *110*, 6474. (b) Nocera, D. G. *Inorg. Chem.* **2009**, *48*, 10001. (c) Lewis, N. S.; Nocera, D. G. *Proc. Natl. Acad. Sci. U.S.A.* **2006**, *103*, 15729. (d) Dau, H.; Limberg, C.; Reier, T.; Risch, M.; Roggan, S.; Strasser, P. *ChemCatChem* **2010**, *2*, 724.

(2) (a) Cukier, R. I.; Nocera, D. G. *Annu. Rev. Phys. Chem.* **1998**, *49*, 337. (b) Huynh, M. H. V.; Meyer, T. J. *Chem. Rev.* **2007**, *107*, 5004. (c) Hammes-Schiffer, S. *Acc. Chem. Res.* **2009**, *42*, 1881. (d) Betley, T. A.; Wu, Q.; Van Voorhis, T.; Nocera, D. G. *Inorg. Chem.* **2008**, *47*, 1849. (e) Betley, T. A.; Surendranath, Y.; Childress, M. V.; Alliger, G. E.; Fu, R.; Cummins, C. C.; Nocera, D. G. *Philos. Trans. R. Soc., B* **2008**, *363*, 1293. (f) Dempsey, J. L.; Esswein, A. J.; Manke, D. R.; Rosenthal, J.; Soper, J. D.; Nocera, D. G. *Inorg. Chem.* **2005**, *44*, 6879. (g) Chang, C. J.; Chang, M. C. Y.; Damrauer, N. H.; Nocera, D. G. *Biochim. Biophys. Acta* **2004**, *1655*, 13.

(3) Esswein, A. J.; McMurdo, M. J.; Ross, P. N.; Bell, A. T.; Tilley, T. D. *J. Phys. Chem. C* **2009**, *113*, 15068.

(4) (a) Cruz, J. C.; Baglio, V.; Siracusano, S.; Ornelas, R.; Ortiz-Frade, L.; Arriaga, L. G.; Antonucci, V.; Arico, A. S. *J. Nanopart. Res.* **2011**, *13*, 1639. (b) Rossmeisl, J.; Qu, Z. W.; Zhu, H.; Kroes, G. J.; Nørskov, J. K. *J. Electroanal. Chem.* **2007**, *607*, 83.

(5) (a) Bockris, J. O.; Otagawa, T. *J. Phys. Chem.* **1983**, *87*, 2960. (b) Suntivich, J.; Gasteiger, H. A.; Yabuuchi, N.; Shao-Horn, Y. *J. Electrochem. Soc.* **2010**, *157*, B1263. (c) Suntivich, J.; May, K. J.; Gasteiger, H. A.; Goodenough, J. B.; Shao-Horn, Y. *Science* **2011**, *334*, 1383.

(6) (a) Kanan, M. W.; Nocera, D. G. *Science* **2008**, *321*, 1072. (b) Surendranath, Y.; Dincă, M.; Nocera, D. G. *J. Am. Chem. Soc.* **2009**, *131*, 2615. (c) Dincă, M.; Surendranath, Y.; Nocera, D. G. *Proc. Natl. Acad. Sci. U.S.A.* **2010**, *107*, 10337. (d) Surendranath, Y.; Lutterman, D. A.; Liu, Y.; Nocera, D. G. *J. Am. Chem. Soc.* **2012**, *134*, 6326.

(7) (a) Kanan, M. W.; Yano, J.; Surendranath, Y.; Dincă, M.; Yachandra, V. K.; Nocera, D. G. *J. Am. Chem. Soc.* **2010**, *132*, 13692. (b) Risch, M.; Khare, V.; Zaharieva, I.; Gerencser, L.; Chernev, P.; Dau, H. *J. Am. Chem. Soc.* **2009**, *131*, 6936. (c) Risch, M.; Klingan, K.; Ehrenberg, D.; Chernev, P.; Zaharieva, I.; Dau, H. *Chem. Commun.* **2011**, *47*, 11912. (d) Bediako, D. K.; Lassalle-Kaiser, B.; Surendranath, Y.; Yano, J.; Yachandra, V. K.; Nocera, D. G. *J. Am. Chem. Soc.* **2012**, *134*, 6801.

(8) Risch, M.; Klingan, K.; Ringle, F.; Chernev, P.; Zaharieva, I.; Fischer, A.; Dau, H. *ChemSusChem* **2012**, *5*, 542.

(9) Chebiam, R. V.; Prado, F.; Manthiram, A. *Chem. Mater.* **2001**, *13*, 2951.

(10) Surendranath, Y.; Kanan, M. W.; Nocera, D. G. *J. Am. Chem. Soc.* **2010**, *132*, 16501.

(11) Young, E. R.; Nocera, D. G.; Bulovic, V. *Energy Environ. Sci.* **2010**, *3*, 1726.

(12) Gardner, G. P.; Go, Y. B.; Robinson, D. M.; Smith, P. F.; Hadermann, J.; Abakumov, A.; Greenblatt, M.; Dismukes, G. C. *Angew. Chem., Int. Ed.* **2012**, *51*, 1616.

(13) Goodenough, J. B.; Kim, Y. *Chem. Mater.* **2010**, *22*, 587.

(14) Lutterman, D. A.; Surendranath, Y.; Nocera, D. G. *J. Am. Chem. Soc.* **2009**, *131*, 3838.

(15) Casey, W. H. *J. Colloid Interface Sci.* **1991**, *146*, 586.

(16) Esswein, A. J.; Surendranath, Y.; Reece, S. Y.; Nocera, D. G. *Energy Environ. Sci.* **2011**, *4*, 499.

(17) Chivot, J.; Mendoza, L.; Mansour, C.; Pauporte, T.; Cassir, M. *Corros. Sci.* **2008**, *50*, 62.